

The Radio-Infrared Nebula in II Zw 40: Clusters Forming in Colliding Elongated Clouds

Dan Beilis^{1*} Sara C. Beck,¹ John Lacy,² Jean L. Turner,³
 Haiyu Baobab Liu,^{4,5} Paul T.P. Ho,⁶ S. Michelle Consiglio³

¹*School of Physics and Astronomy, Tel Aviv University, Ramat Aviv, Israel 69978*

²*Department of Astronomy, University of Texas, Austin Tx USA*

³*Department of Astronomy, UCLA, Los Angeles, Ca. USA*

⁴*Department of Physics, National Sun Yat-Sen University, No. 70, Lien-Hai Road, Kaohsiung City 80424, Taiwan, R.O.C.*

⁵*Center of Astronomy and Gravitation, National Taiwan Normal University, Taipei 116, Taiwan*

⁶*Academica Sinica Institute of Astronomy and Astrophysics, Taipei, Taiwan*

Accepted XXX. Received YYY; in original form ZZZ

ABSTRACT

II Zw 40 is a starburst dwarf and merger product, and holds a radio-infrared supernebula excited by thousands of embedded OB stars. We present here observations of three aspects of the supernebula: maps of the K and KU radio continuum that trace dense ionized gas with spatial resolution $\sim 0.1''$, a spectral data cube of the [S IV] $10.5\mu\text{m}$ emission line that measures the kinematics of the ionized gas with velocity resolution 4.5 km s^{-1} , and an ALMA spectral cube of the CO(3-2) line that probes the dense warm molecular gas with spatial and velocity resolution comparable to the ionized gas. The observations suggest that the supernebula is the overlap, collision or merger of two star clusters, each associated with an elongated molecular cloud. We accordingly modelled the supernebula with simulations of colliding clusters. The model that best agrees with the data is a grazing collision that has distorted the gas and stars to create the distinctive structures observed. These models may have wide applicability in the cluster-rich regions of young starbursts.

Key words: galaxies: individual (II Zw 40) — galaxies: starburst — galaxies: star clusters: general — methods: numerical

1 INTRODUCTION

II Zw 40 is a peculiar blue compact dwarf galaxy 10.3 Mpc distant and the prototype ‘Extragalactic H II Region’ (Sargent & Searle (1970), Searle & Sargent (1972)). It is believed to be the product of a merger between two dwarf galaxies and that the merger has triggered the starburst. The optical emission is dominated by a giant H II region $\sim 7''$, 350 pc diameter holding many young star clusters. The two brightest clusters are referred to as SSC-N and SSC-S or Sources A,B (Kepley et al. (2014), Vanzi et al. (2008)). SSC-N is the brighter by a factor of 20 and is the dominant energy source of the H II region. The luminosity and mass of SSC-N deduced from optical and UV observations are an order of magnitude greater than those of 30 Doradus ($9.1 \pm 1 \times 10^5 M_{\odot}$, $1.1 \pm 0.1 \times 10^9 L_{\odot}$, (Leitherer et al. 2018)). At longer wavelengths the central region of II Zw 40 is dominated by a radio-infrared supernebula excited by thousands of embedded O stars (Beck et al. (2002), Kepley et al. (2014)). The spatial structure of the emission is not simple; the 6-1.3 cm observations of Beck et al. (2002) and Kepley et al. (2014) found multiple clumps which they interpreted as sub-clusters but the clumps were at the edge of detectability, depended very much on the deconvolution parameters, and were not consistent between the various maps.

As in many low-metallicity galaxies, CO(1-0) in II Zw 40 is very

weak and hard to observe (Sage et al. 1992). The higher level CO lines are stronger; Consiglio et al. (2016) show high-resolution CO(3-2) maps made with ALMA, and Kepley et al. (2016) report CO(3-2) and (2-1) maps. The CO is concentrated into small clouds, one of which coincides with the radio-infrared source. Kepley et al. (2016) find clumps at multiple velocities over a total range of $\approx 30\text{ km s}^{-1}$, with most of the molecular emission at $750 \pm 10\text{ km s}^{-1}$, close to the galactic velocity of 773 km s^{-1} (derived from stars, Mould et al. (2000); the HI velocity is 800 km s^{-1} , Springob et al. (2005)). The small CO clouds are not seen to be directly related to the atomic and molecular structures seen at larger scales.

Optical and near-IR observations of shocked and ionized gas in the starburst region find gas motions strongly affected by the energetic activity of the young stars (Bordalo et al. (2009b)); Vanzi et al. (2008) do not find any connection to the dynamics and structure of the galaxy on larger scales. There are convincing arguments that the starburst was triggered by cloud-cloud collisions as the two dwarf galaxies merged; the tidal tails observed in HI (van Zee et al. 1995) are witness to this history. On scales of the starburst, winds and outflows of the young stars have muted traces of these interactions.

Observations of the central $\sim 300\text{ pc}$ of II Zw 40, as summarized above, present a picture of a region where star clusters have very recently been born. In this paper we attempt to deduce the history of the current active starburst (that centered on the radio-infrared supernebula). We address this question from two angles. We first

* danbeilis@mail.tau.ac.il

present new high spectral and spatial resolution observations of the dense and compact components of the ionized gas. This gas is directly associated with the bright, embedded and young star clusters rather than with the giant H II region. The new data probes the density distribution of gas and stars inside the clusters as well as the motion of the gas ionized by the young stars. We combine this new data with CO(3-2) ALMA observations of the molecular gas in which the youngest clusters are embedded. This data reveals the immediate kinematic environment of the starburst and the molecular gas which fuels it. The observations are detailed in Section 2, the spatial structure of the ionized gas and molecular gas in Section 3, and the kinematics of ionized and molecular gas in section 4. The observations motivate the second aspect of the paper, wherein we model the II Zw 40 starburst as the collision of two star clusters which have formed in two elongated molecular clouds. We have run simulations of colliding and interacting molecular clumps and of star clusters merging under a wide range of conditions, which are discussed in Section 5. In Section 6 we compare our simulations to the observations, arrive at a favoured model, and predict the future development of the II Zw 40 clusters.

2 OBSERVATIONS AND DATA REDUCTION

2.1 Radio Continuum Maps

II Zw 40 was observed in JVLA project 16B-067. The K-band (22 GHz) observations were carried out on 15 October 2016 and Ku (15 GHz) on 31 October 2016. Total execution times were 00:43:06 and 00:54:16, and the bandpasses 6 GHz, 4GHz respectively. The data was handled with the standard JVLA pipeline process¹, version 4.7.1, and since in this time period the atmospheric delay model was not applied properly² all data from affected observations were re-processed with a corrected model. The data were cleaned and imaged with CASA and AIPS. The galaxy was mapped with natural weighting for greatest sensitivity and Briggs weighting (robust = 0) for higher resolution. The observational parameters are given in Table 1.

2.2 Mid-Infrared Spectroscopy with TEXES

II Zw 40 has low metallicity and high excitation (Leitherer et al. 2018) and its mid-infrared spectrum, as seen by the Spitzer IRS (Wu et al. 2006), is dominated by the high excitation lines of [NeIII] 15.5 μm and [S IV] 10.5 μm . [NeIII] cannot be observed from the ground so [S IV] is used to probe the ionized gas kinematics (Beck et al. 2013). [S IV] has two great advantages over H I recombination lines; it is less affected by extinction than many, including Bry, and it is much less affected by thermal broadening than any hydrogen line can be. Thermal broadening in an H II region at $T_e \sim 10^4\text{K}$ will give any hydrogen line FWHM about 20 km s^{-1} , while a line of a metal of mass m_i will have width $\sqrt{\frac{m_{\text{H}}}{m_i}}$ \times that of hydrogen.

We accordingly observed [S IV] in II Zw 40 with the TEXES spectrometer on Gemini North on 15 March 2017. TEXES, the Texas Echelon Cross Echelle Spectrograph (Lacy et al. 2002), operates between 4.5 and 25 μm and has spectral resolution $R \approx 4000-100,000$. These observations were performed in high resolution mode, using a

32 line/mm echelle and a 0.5'' wide, 4'' long slit. The S^{+++} thermal broadening of $\approx 3.5 \text{ km s}^{-1}$, added in quadrature to the instrumental resolution, gives the true resolution of $\approx 4.5 \text{ km s}^{-1}$. The asteroid Vesta was the calibrator. The slit was aligned north-south and stepped east-west across the targets and the scan combined into a data cube of 23 0.25'' pixels in R.A., 32 0.14'' in Dec, and 256 0.95 km s^{-1} wide velocity channels.

2.3 Archival ALMA Observations of Molecular Gas

II Zw 40 was observed in ALMA Band 7, 345 GHz, as a Cycle 2 (Early Science) program (ID = 2013.1.00122.S). Band 7 observations took place on 2014 13 August and 13 December; weather conditions were good, with $T_{\text{sys}} = 140-250 \text{ K}$ and PWV $\sim 0.78\text{mm}$. Observations of a single field with an 18'' field-of-view centered on 05:55:42.620 +03:23.32.0 (no offset) were concatenated with total time 2844 seconds on source. Bandpass and phase were calibrated with J0607-0834 and J0532+0732 respectively; J0510+180 was the flux calibrator. Calibration of the data was done in the pipeline³ and with CASA 4.2.2. Continuum emission was subtracted in the (u,v) plane before making line maps.

3 SPATIAL DISTRIBUTION OF MOLECULAR AND IONIZED GAS IN THE STARBURST

3.1 Radio Continuum: Multiple Clusters?

Figures 1a+b and 1c show II Zw 40 at 15 and 22 GHz. The source has an extended emission envelope with some clumpy structure, dominated by a bright source at RA 05:55:42.60 DEC 03:23:32.0. This position agrees with Kepley et al. (2014)'s Source D and with their position for SSC-N. It is the only distinct emission peak. The highest resolution radio map, Figure 1c, has a 0.12'' beam and shows the bright clump to be resolved with size 0.13'' or $\approx 6.5 \text{ pc}$ (in both axes) and flux 0.59 mJy. The JVLA maps, which are deeper than those of Beck et al. (2002) and have noise lower by a factor ≈ 5 , show a rather different picture of the embedded HII regions. Where Beck et al. (2002) saw $\approx 2\sigma$ brightness fluctuations as possible secondary clusters and could not detect most of the extended emission, the current data show that ionized gas has an unusual and asymmetric extended structure and that the spatial distribution is dominated by one large cluster.

3.1.1 The [S IV] Agrees with the Radio Continuum

Figure 1d shows the [S IV] emission summed over the entire grating order, covering velocities from 600 to 880 km s^{-1} . The TEXES beam size at Gemini was $\sim 0.3''$, close to the diffraction limit; the pixel size, set by the scan method, was $0.25 \times 0.144''$. Comparing the [S IV] map to the 15 GHz radio map of Figure 1a, which has close to the same resolution, shows very similar spatial distribution. This confirms that the [S IV] emission is closely associated with the embedded star cluster which excites the radio continuum peak, and is not affected by emission of the larger optically bright H II region.

¹ <https://science.nrao.edu/facilities/vla/data-processing/pipeline>

² <https://science.nrao.edu/facilities/vla/data-processing/vla-atmospheric-delay-problem>

³ <https://almascience.eso.org/processing/science-pipeline>

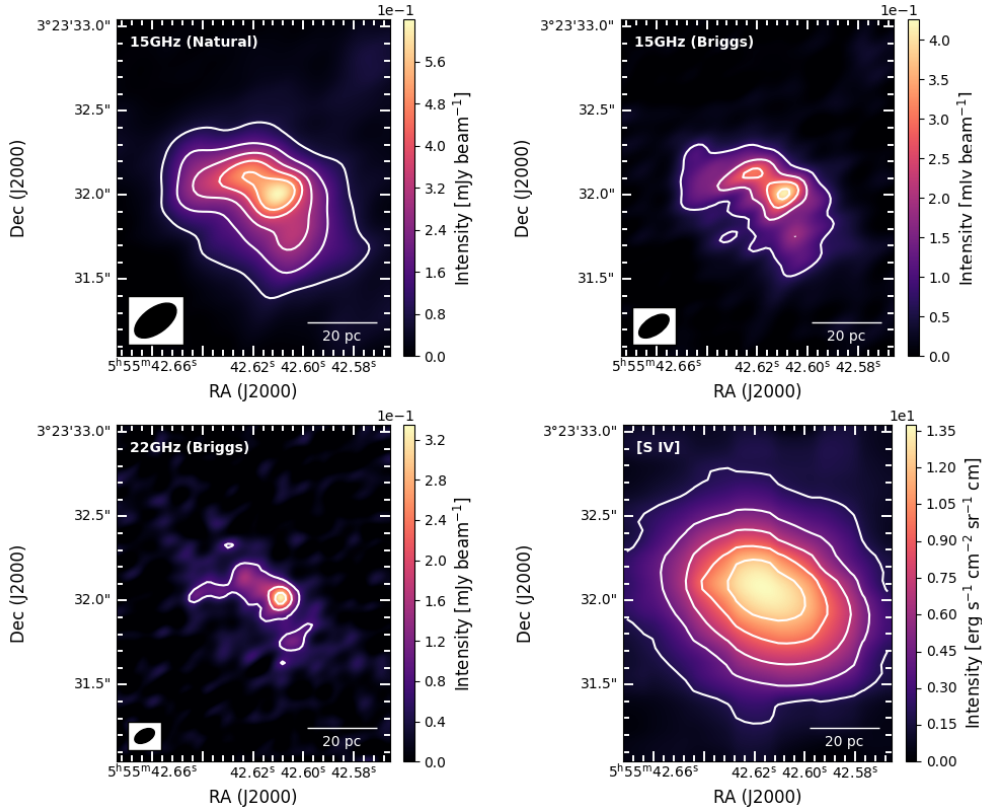


Figure 1. II Zw 40 imaged at (clockwise from upper left): a) 15 GHz (natural weight), b) 15 GHz (Briggs weight), c) 22 GHz (Briggs weight), d) [S IV] 10.5 μm , 0.3'' beam. The intensity wedges have units mJy beam^{-1} for the radio and $\text{erg s}^{-1} \text{cm}^{-2} \text{sr}^{-1} \text{cm}$ for the [S IV] and the contours levels are [0.8,1.85,2.9,3.95,5] for the radio maps and [2,4.5,7,9.5,12] for the [S IV].

3.2 Spatial Structure of Dense Molecular Gas

Figure 2 displays the first 3 moments of the CO(3-2) data cube (integrated line intensity, intensity-weighted velocity, and velocity dispersion). The 4th panel of the figure shows the integrated [S IV] line intensity overlaid on the molecular gas distribution. The molecular gas has larger extent than does the ionized and is distributed in several distinct density peaks. The dominant molecular peak marked as 'W4' in Figure 6, agrees with Consiglio et al. (2017)'s CO and 3 mm continuum peak 'W', and is co-incident with the radio and infrared cluster. NE of this peak emission of the ionized gas drops off sharply at the border of Consiglio et al. (2017)'s component 'C' ('W3' in Figure 6). The spatial distribution of the high-resolution Briggs radio map suggests that the radio emission is blocked from extending into component 'C'; if real and not an artifact of the display, this may show a high density ionization front. We do not detect ionized gas in Consiglio et al. (2017)'s source 'E' ('E' in 6).

4 GAS KINEMATICS IN THE STARBURST

4.1 Ionized Gas: Double Peak or Extended Wing?

Beck et al. (2013) observed II Zw 40 with TEXES at the NASA IRTF and obtained spectra with 1.2'' spatial resolution. They found that the [S IV] line emission extended to high velocities redwards of the peak and that the line profile could be fit by two gaussians separated in velocity by $\approx 44 \text{ km s}^{-1}$. Beck et al. (2013) accordingly suggested that two super star clusters offset in velocity were included

in the same beam, a model which motivated the higher resolution observations of Gemini.

Figure 3 shows the Gemini [S IV] line profile summed over the entire source. The new data confirm that 1) the line peaks at $745 \pm 5 \text{ km s}^{-1}$, 2) emission covers an extraordinarily large velocity range of $\sim 130 \text{ km s}^{-1}$ FWZI, and 3) the line profile is extremely asymmetric, extending to $\sim 100 \text{ km s}^{-1}$ red and only $\sim 50 \text{ km s}^{-1}$ blue from the peak with excess emission on the red side of the line peak. The line profile could be formally fit by 2 gaussians at $\sim 744, 775 \text{ km s}^{-1}$ consistent with the IRTF results⁴, although it does not rule out large scale gas flows in addition to the two peaks.

The simplest interpretation of the line profile is that the source holds two clusters, the larger ≈ 2 times the brightness of the smaller. If this is so, can we see any sign of the second cluster in the spatial distribution of the ionized gas? If the red excess is associated with one of the sub-clumps seen in the high resolution JVLA and ALMA maps it would support the model of two off-set clusters.

Figure 4 displays the [S IV] data cube collapsed along the velocity (moment 0), R.A. and Declination axes. Both components are extended. Examining the line profiles in each pixel (as in the Appendix figure) confirms that both features appear in every pixel and that the blue is the stronger except for a small area of the extreme south-east where the red dominates. But in none of the radio or infrared maps

⁴ The [S IV] velocities given in Beck et al. (2013) differ from those here because they were on a geocentric, not heliocentric, system.

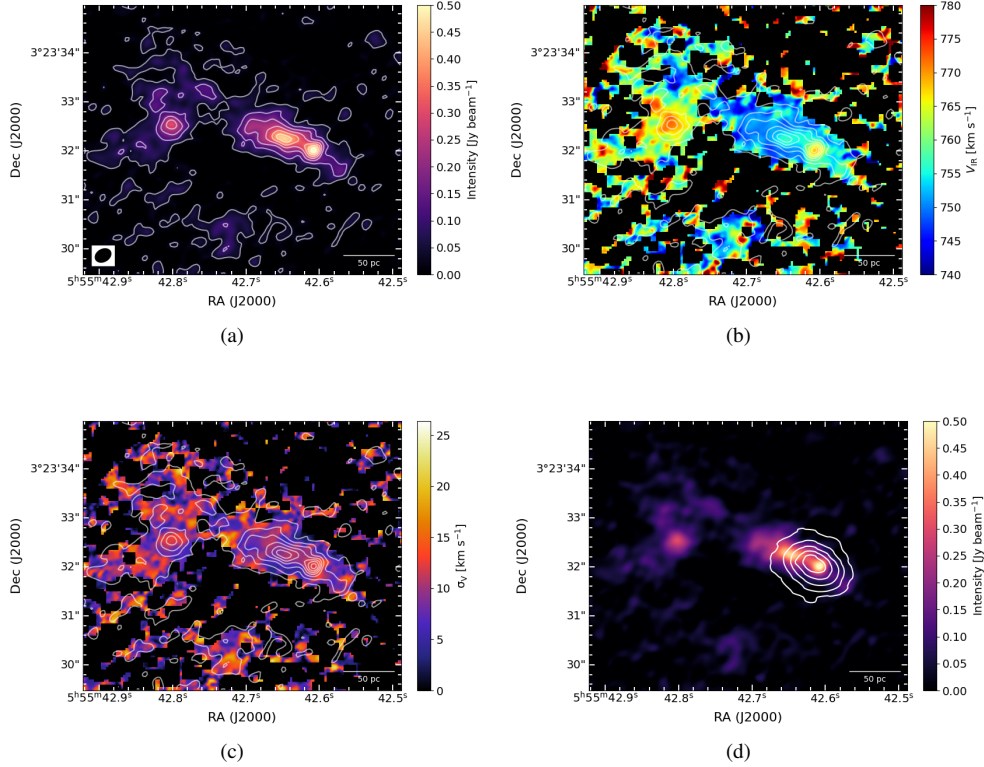


Figure 2. II Zw 40 SSC-N CO(3-2) (a) 0th moment map with contours at [0.03, 0.11, 0.19, 0.26, 0.34, 0.42, 0.5] Jy beam⁻¹, (b) 1st moment map, (c) 2nd moment map and (d) 0th moment map with [S IV] contours at [2,4,5,7,9,5,12] erg s⁻¹ cm⁻² sr⁻¹ cm. The maps in panels a,b, and c are overlaid with the CO 0th moment map contours.

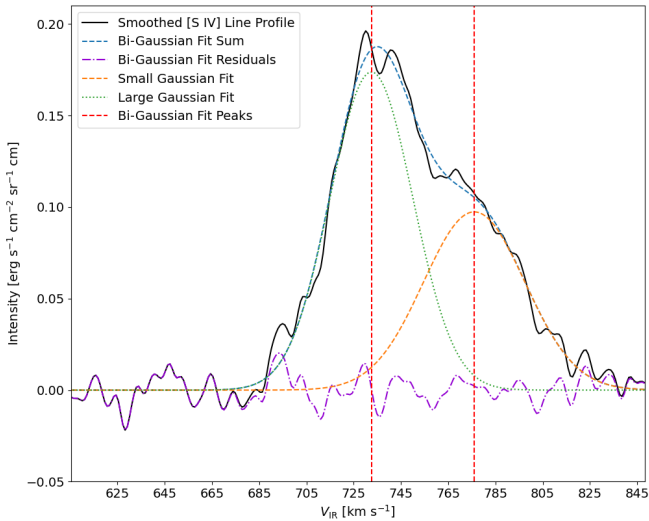


Figure 3. [S IV] emission summed over entire source, smoothed by 3 pixels (1 resolution element). X axis units are km s⁻¹ and Y axis units are erg s⁻¹ cm⁻² sr⁻¹ cm

of the ionized gas is there a spatial density peak or clump associated with the red emission.

We conclude that if there are two distinct clusters, as the [S IV] profile strongly suggests, they so overlap in the line of sight that they cannot be separated.

4.2 Molecular Gas: Two Elongated Clouds at Different Velocities

Figure 5 shows the CO data cube collapsed along the velocity, declination and right ascension axes, and together with Figure 2 demonstrates that both the intensity-weighted velocity and the dispersion of the CO line are larger going from east to west along the streamer and reach maxima on the radio source. The line profile (shown in Figure 6) also varies markedly over this region. In the eastern clump (Feature E of [Consiglio et al. \(2017\)](#)) the profile is flat-topped, almost rectangular, and covers $\sim 750 - 780$ km s⁻¹. In the main molecular streamer that includes the radio and [S IV] sources, two velocity features appear along the length of the emission. The blue peak is consistently at $\sim 745 - 750$ km s⁻¹ and the red varies between $\sim 760 - 772$ km s⁻¹; the profile on the radio-[S IV] source resembles that of the [S IV] line but does not extend quite as far into the red. (These velocity features can be seen also in the channel maps in the Appendix).

The Position-Velocity diagram (PVD) along the Dec axis resembles the V-shape observational signature of a cloud-cloud collision [Torii et al. \(2017\)](#) (highlighted in a subfigure in Figure 5). This shape would usually be skewed when observed at an inclination angle. That the Dec PVD appears closer to a check mark than a 'V' may indicate that a more complex collision is occurring.

More insight into this complicated velocity field may be found in the Position-Velocity Diagrams (PVDs) of Figure 7 (As the molecular source E is not associated with embedded star formation it will not be included in the rest of this discussion). The PVDs are consistent

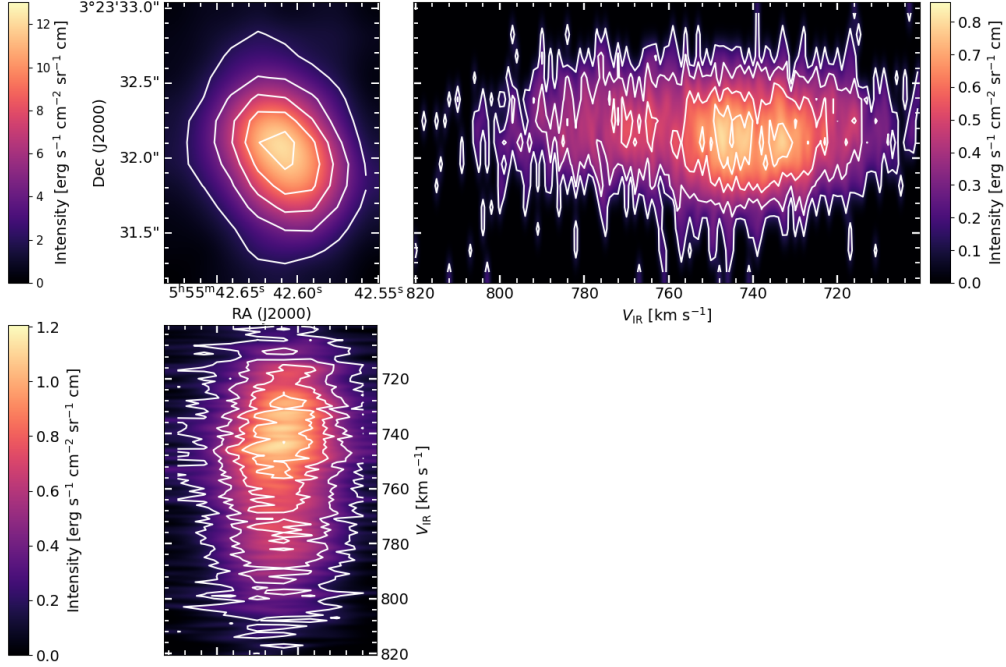


Figure 4. The [S IV] data cube collapsed along the axis of velocity (top left), R.A. (top right) and Dec. (bottom). Emission redder than $\approx 745 \text{ km s}^{-1}$ is slightly asymmetric in Declination, extending further south. The contours for the top, right and bottom subfigures are respectively [2,4,5,7,9,5,12], [0.15,0.34,0.53,0.71,0.9] and [0.2,0.45,0.7,0.95,1.2] $\text{erg s}^{-1} \text{ cm}^{-2} \text{ sr}^{-1} \text{ cm}$

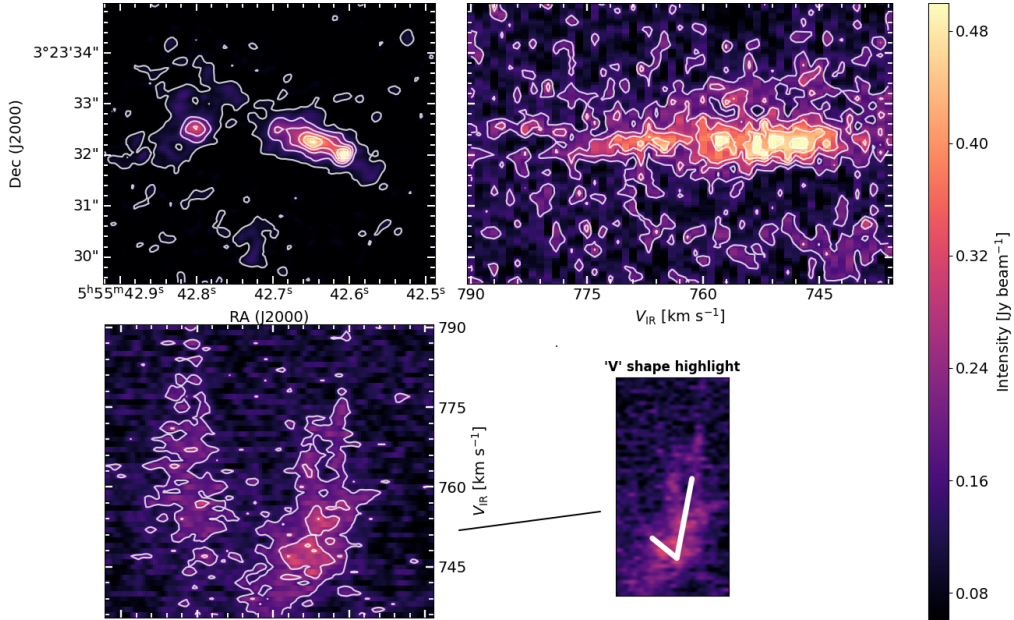


Figure 5. The CO(3-2) data cube collapsed along the axis of velocity (top left), R.A. (top right) and Dec. (bottom left). The contours are at [0.08, 0.16, 0.24, 0.32, 0.4, 0.48] Jy beam^{-1} . (bottom right) The western cloud, indicated by the pointer line in the previous figure, expanded and marked in white to highlight the potential observational signature of a cloud-cloud collision [Torii et al. \(2017\)](#).

with two elongated clouds overlapping in the line of sight, consistent with the double line peaks of Figure 5. This motivates the working

picture of II Zw 40 which we will explore with the simulations of the next section.⁵

⁵ Note that the CO and [S IV] velocities do not agree with the $H\alpha$ velocities observed by [Bordalo et al. \(2009a\)](#), which are close to 780 km s^{-1} over

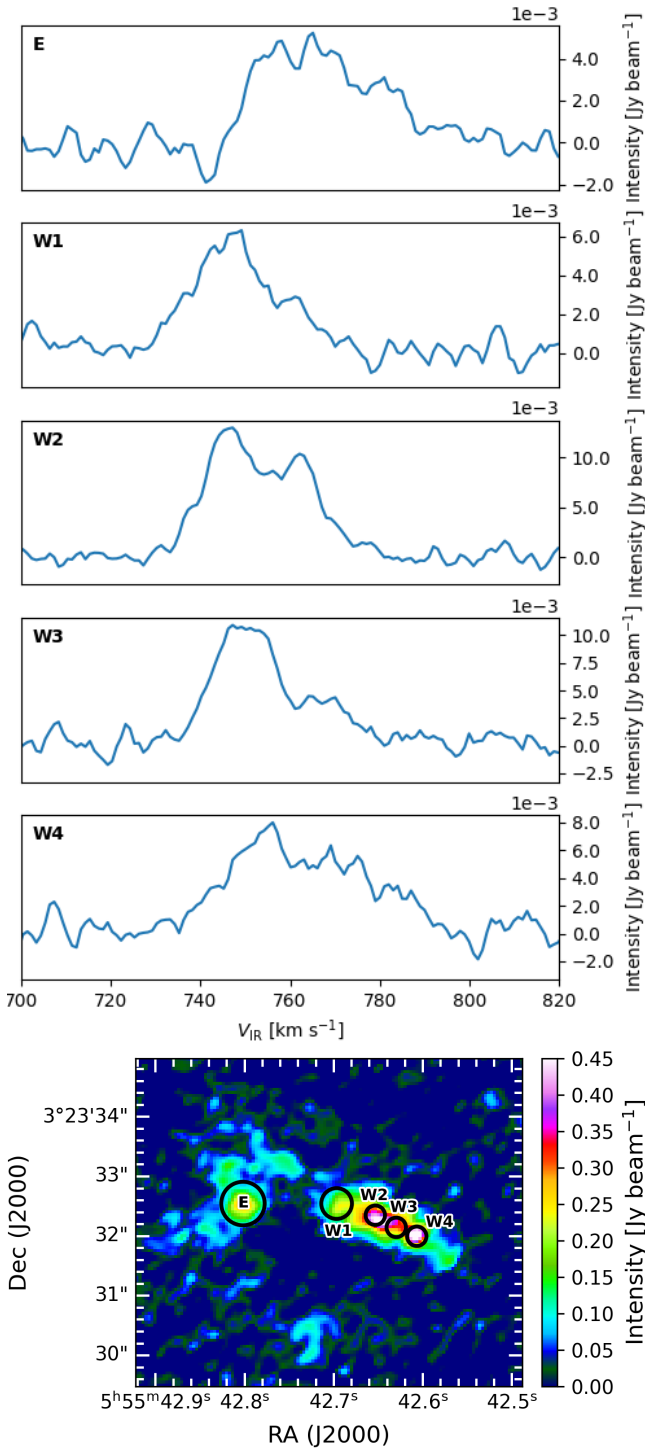


Figure 6. Top, line profiles of CO(3-2) in 5 positions across the source. Bottom, the MOM0 map of CO(3-2) with circles identifying the location and showing the area over which the data was summed for each line profile.

the entire emission region; the optical velocity field is highly complex and dominated by large expanding bubbles.

5 SIMULATIONS: COLLIDING/MERGING CLUSTERS AND CLUMPS

The infrared, radio, and sub-millimeter observations reported combine to show that the II Zw 40 core holds two elongated molecular clouds that overlap in the line of sight, and to suggest strongly that two star clusters at different velocities, also overlapping in the line of sight, are present. The active star formation region with the embedded star cluster(s) is at one end of the spatially overlapping elongated molecular clouds, where the line profiles of the clouds merge to form a single broad feature. These observations strongly suggest that the clouds are colliding or merging on the west end and that the star formation is concentrated in the collision region. This has motivated us to model the II Zw 40 starburst with simulations of colliding clusters.

Theoretical calculations and models (extensive work including Takahira et al. (2018), Habe & Ohta (1992) and references therein) have established that the increased gas pressure in colliding clouds can increase or trigger star formation. Such collisions are probably the main mechanism of the starbursts in interacting galaxies. It has however been very difficult to observe collision-induced star cluster formation directly. As soon as the young stars turn on, their winds and radiation start to disperse the surrounding clouds, so there is only a short ($\sim 2\text{Myr}$, Fukui et al. (2016)) time in which the collision and star formation processes can be observed. We are fortunate that II Zw 40 appears to be now at exactly the stage where massive young stars have formed but enough of the natal clouds remain that we can model their interaction. We accordingly have developed code to simulate cluster formation in clump collision and use it to reproduce as well as possible the observations of II Zw 40. In the next sections we briefly describe the numerical methods, the results, and the model we believe to best explain II Zw 40.

5.1 Numerical Methods: the AMUSE Environment

A full picture of the embedded clusters in II Zw 40 must consider hydrodynamics of the gas, gravitational interactions of the stars and of the stars with the gas, the evolution of the embedded stars and the effects of their winds (and ideally the magnetic field, for which there is at present no data). The Astrophysical Multipurpose Software Environment (AMUSE) assembles community codes and makes it possible to run computations of all these aspects in parallel and to communicate the results between codes. AMUSE couples all the codes, N-body and hydrodynamical, via a Bridge scheme (Fujii et al. 2007). For these simulations we used the community codes ph4 (Dolcetta et al. 2011) for the N-body calculations and GADGET-2 (Springel 2005) for Tree-SPH calculations. We follow the evolution of the cluster stars with the parameterized stellar evolution module SeBA (Portegies Zwart & McMillan 2018), which gives stellar radius, luminosity and temperature as functions of time. SeBA returns a mass loss rate from stellar winds which, input to the AMUSE stellar winds module (van der Helm et al. 2019), generates more particles for the SPH calculations. Stellar winds are expected to develop very differently in dense embedded clusters than in the field (Wunsch et al. 2011); we accordingly use the stellar wind module's 'heat' mode, which follows the energy rather than the velocity of the wind particles, as most appropriate for this embedded source.

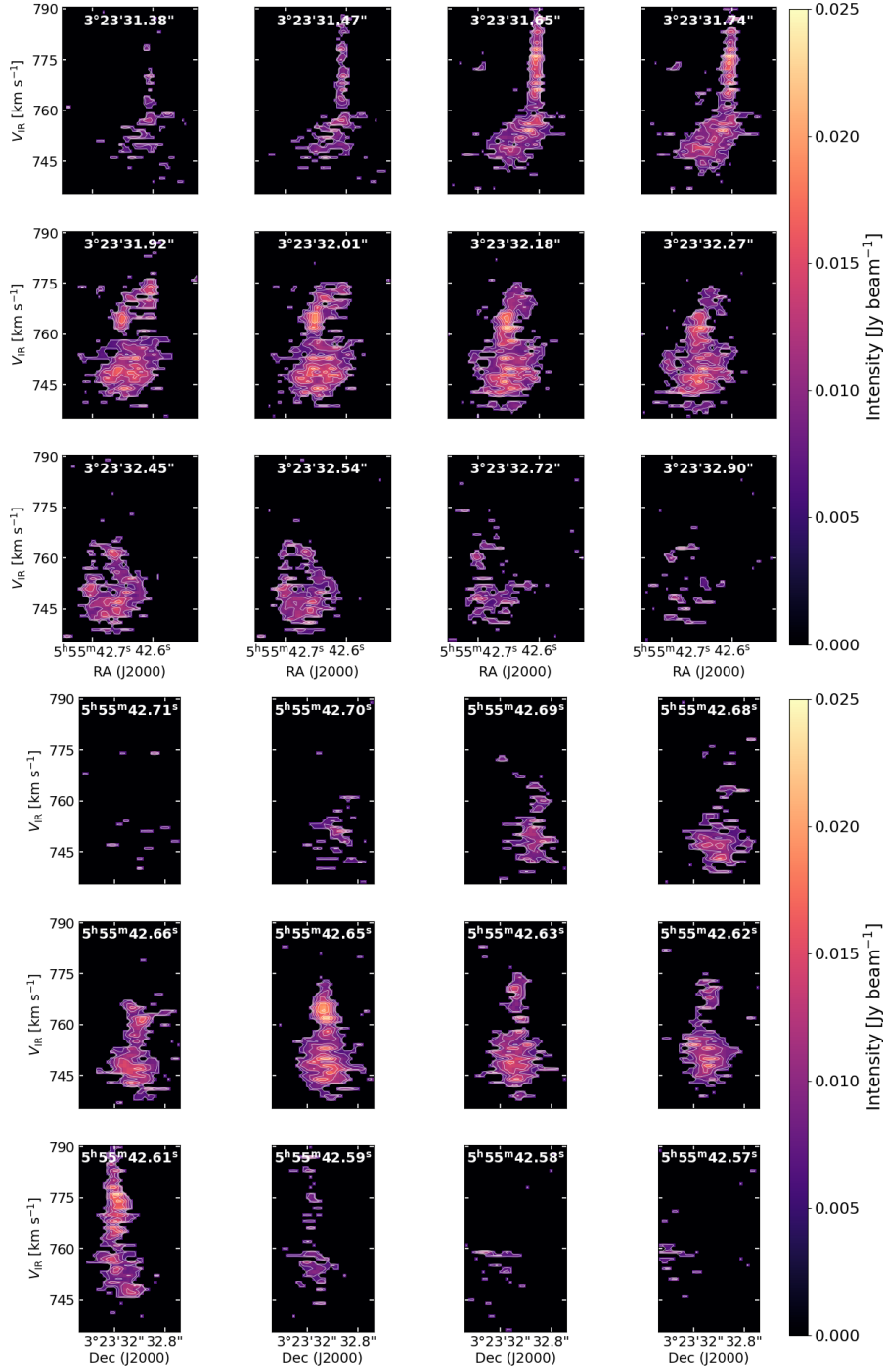


Figure 7. Position-Velocity Diagrams of the CO(3-2) observations along the Dec axis (top) and the RA axis (bottom). The contours are at [0.005, 0.0075, 0.01, 0.0125, 0.015, 0.0175, 0.02] Jy beam⁻¹.

5.2 Simulations

5.2.1 Cluster Evolution

Our observations show that the great cluster SSC-N coincides with the spatial overlap of two elongated molecular clouds, and establish the line-of-sight velocity offset of the clouds. This motivates us to model SSC-N as the result of the cloud's interaction. In this paper we start with the assumption that a star cluster has already formed

in each clump, and follow the appearance of the resulting system through the collision. (We intend in future work to examine separately the alternate case of star formation starting after the collision). The collision thus starts with physically realistic clusters, rather than with an assumed density and velocity distribution. We estimate from the line profile that the larger cluster is roughly twice the mass of the smaller, and from the total ionizing flux N_{Lyc} of SSC-N that the total populations of massive O stars are approximately 4300, 2150 O

stars respectively. The model clusters therefore have total masses of $4.5 \times 10^5 M_{\odot}$ and $2.2 \times 10^5 M_{\odot}$ where we assumed the gas comprises 70% of the total mass as the star formation efficiency in SSCs is often quite high (Lada & Lada 2003).

The initial conditions were chosen to be typical of stellar clusters: for the gas we assumed an idealized Plummer sphere Plummer (1911), a Maxwell-Boltzman velocity distribution matching a temperature of $T = 10^4$ K and a particle mass of $1.5 M_{\odot}$. For the stars, we assumed a King model King (1966) and a Salpeter initial mass function Salpeter (1955) in a mass range of $[15, 120] M_{\odot}$. We chose these 'top heavy' mass limits to keep the total stellar mass and the computational demands realistic; the winds of low mass stars are so much weaker than those of massive stars that they can be omitted with little effect on the large-scale results. The clusters were allowed to evolve for a total of 2 Myr with a 10 kyr timestep. We chose the total evolution time based on the maximum dynamical relaxation time of the gas for both clusters based on their mass, number of particles and virial radius Spitzer (1987). In each timestep, the stellar evolution module was allowed to evolve for half a timestep each time as it required a higher temporal resolution, then the bridge code (combining the gravitational and hydrodynamical code modules) and stellar wind module was allowed to evolve for a full timestep and finally the stellar evolution module was allowed to evolve for an additional half timestep. After each code module ran, the appropriately affected parameters were copied from one code module to the other using the AMUSE inter-module communication scheme.

After the evolution of each cluster, we examined the rate of mass loss (SPH particles blown away due to the stellar winds), radius, mass and energy to make sure that they were behaving in a typical manner of stellar clusters. This also helped us determine the best AMUSE modules for our purposes and what settings to run them at; The stellar wind module was set to the 'heating' kind based on the results of van der Helm et al. (2019) and confirmed by examining the radius and number of SPH particles blown away by each stellar wind mode. Additionally, the mass of the SPH particles was chosen by running the cluster evolutions using different masses and determining which one provided the sufficient accuracy for our case.

5.2.2 Cluster Collision

The simulations of cluster collisions were run exactly the same way as the cluster evolutions, including both stellar evolution and stellar winds. The clusters were then trimmed to a little over the virial radius of each (which was also higher than the half-mass radius). This resulted in clusters that still had a large percent of the original gas while also preserving the core and outer layer structure. The primary reason for doing so was to reduce the run-time of the collision simulations while still maintaining sufficient approximations of realistic cluster structures and gas and stellar mass order of magnitudes estimated for the colliding clusters in II Zw 40. In addition, the main focus in these simulations was to find a match to the two velocity peaks, to which the cores of the colliding clusters are the most important contributions.

For the actual collision, the large cluster was placed at the center of the coordinates system and the small cluster was set some distance away with initial velocity of approximately 120 km s^{-1} . This velocity was determined by running multiple low-scale simulations, approximating the resulting line profile, and comparing it to the [S IV] line profile. The small cluster was then set to move at an angle so as to result in an approximately horizontal distribution of the two clusters relative to each other after the collision (see Figure 9). The impact parameter b , defined as the distance between the cluster centers, is crucial in determining the outcome of the collision. We ran simu-

lations for a range of b starting from 0, the head-on collision, and increasing by 0.5 pc increments to 6 pc, where the cluster interaction is minimal.

The time step is the same as in the evolution simulations, 10^4 yr, and the total runtime for each collision was 0.5 Myr. After all the collisions were finished, the AMUSE results were used as input for the radiative transfer software RADMC-3D Dullemond et al. (2012) to produce 3D line profiles. For the stars this included their mass, radius, temperature and position, and for the gas their mass, velocity and position. The properties of the SPH gas particles were interpolated to a grid of size $256 \times 256 \times 256$ that covered the entire range of gas distribution which was $60 \times 60 \times 60$ pc. Each collision was observed at an inclination angle of 45, 60 and 75°, as these angles gave a better line profiles match to the original [S IV] observations. The 3D line profile simulations were made in both CO(3-2) and [S IV].

5.3 Results

5.3.1 Cluster Evolution

The first step of the modelling was to follow the evolution of the clusters before the collision; the results are shown in Figure 8. We find that the stellar winds were the most significant factor in shaping the clusters, which is consistent with the results of simulations run by (Pelupessy & Portegies Zwart 2012); they blew away some of the gas particles, resulting in an overall increase of the clusters radii, and a decrease in the gas density, temperature and average rms velocity. This occurred in both clusters and significantly altered the shape of the larger cluster. The outer regions of the larger cluster are visibly distorted; the higher density small cluster remains mostly spherically symmetric. As the initial model was very general (with the one major omission of not yet including magnetic field effects) we expect these findings to be valid for typical clusters.

5.3.2 Cluster Collision

The density and distribution of gas and stars found from the simulations is shown in Figure 9 for impact parameters of 0-6 pc in the timespan of 0 to 0.5 Myr. The first point to note in this figure is how the impact parameter determines the shape of the gas distribution. In head-on collisions, the small cluster drags gas from the large cluster and spreads it out in a thick wedge-shaped tail. The stellar distribution also changes; the small cluster's distribution becomes more ellipsoidal, while the larger cluster's stays spherical and spreads to a slightly larger radius. In the grazing ($b = 4$ pc) collision, both clusters maintain their overall cohesiveness but each cluster's gas spreads out across the growing divide between the two, resulting in a lower average density. This pattern is repeated at all impact parameters > 2 pc, as can be seen in the Appendix Figure. The stellar distributions do not change drastically.

Comparing the CO 0th moment map and PVDs at different impact parameters displayed in Figure 10, shows that as the impact parameter increases the larger cluster becomes more distinct from the small one both spatially and kinematically. This is related to the gas distribution change pattern in the density distribution seen in Figure 9. As the impact parameter increases, less gas is stripped by the collision, and the clusters become deformed but still remain cohesive. If we consider the kinematic distribution seen in the CO PVDs and [S IV] line profile, the kinematic distance between the two clusters remains constant for increasing impact parameters and at different timesteps. The ratio between the two peaks is the major change,

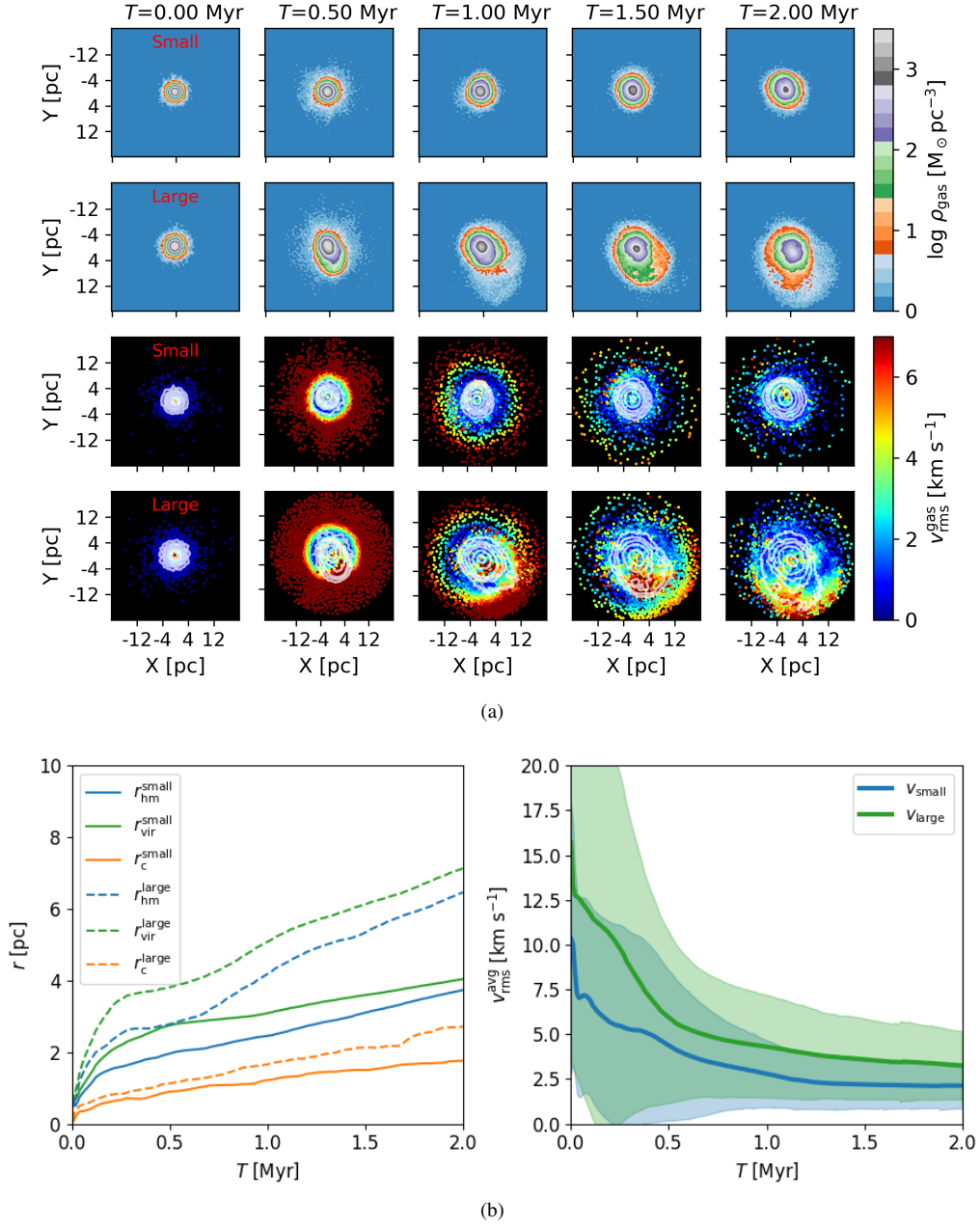


Figure 8. Results of cluster evolution for the small and large clusters in a 10pc slice taken at the center of the Z axis at multiple timesteps (each column shows a different timestep). (a) Top two rows show the density structure (upper: small cluster, lower: large cluster). Bottom two rows show the average rms velocity structure with an overlay of the density structure contours (upper: small cluster, lower: large cluster). (b) Left: shows the half-mass, virial and core radii over time for both clusters. Right: shows the the average rms velocity with standard deviation wings over time for both clusters.

which increasingly favors the small cluster as the impact parameter rises. The other important factor is the inclination observation angle, which changes the spatial and kinematic distance between the two peaks as can be seen in Figure 14. When comparing the CO and [S IV] observations to all the simulation results, specifically in terms of the the overall shape of the two peaks, the spatial and kinematic distance between them and the ratio between the two peaks in the line profile. We determine that the best match to the CO and [S IV] observations occurs for the $b = 4\text{pc}$ impact parameter, at the $T = 0.5\text{Myr}$ timestep, when observed at a 45° inclination angle. We note that while the simulations were made to model mainly the ionized gas distribution, the large scale behaviour of gas in these

conditions, in terms of the spatial distribution and kinematics, would be very similar in the CO and [S IV] as they roughly trace the same gas mass.

6 DISCUSSION

6.1 Clusters in II Zw 40 as Modelled: Positions, Trajectories, and Possible Future Development

The left subfigure in Figure 11 shows the CO integrated line intensity or moment 0 (MOM0) map overlaid with the contours of the [S IV]

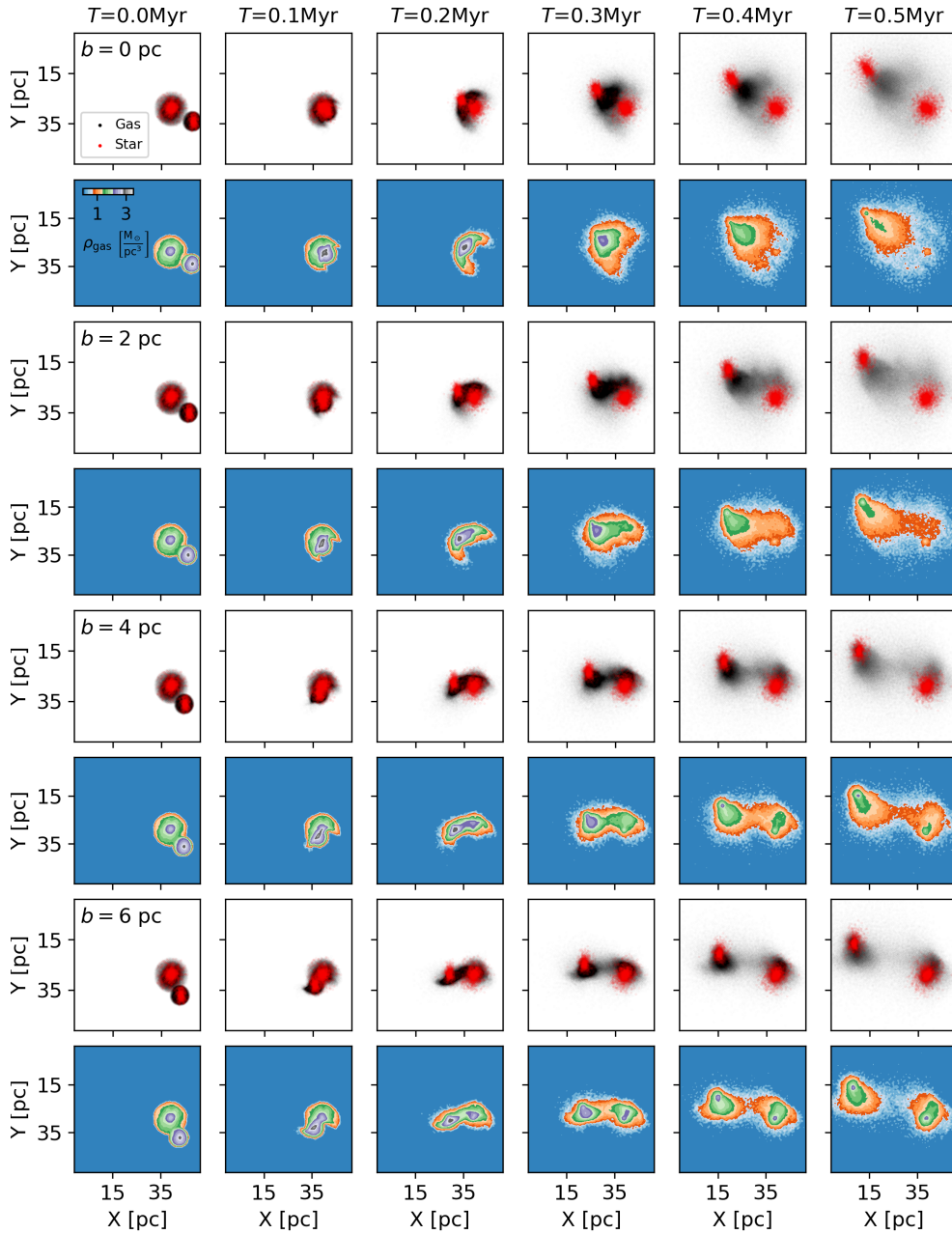


Figure 9. Cluster collision density comparison for two impact parameters at multiple timesteps; each column is a different timestep. Every pair of rows shows the collision results for a different impact parameter ranging from $b = 0$ to 6 pc (where the density scale is $[0, 3.5]M_{\odot} \text{pc}^{-3}$). The odd rows show the distribution of the gas SPH particles and the stars as black and red dots respectively. The even rows show the average gas density in a 10 pc slice along the Z axis.

and radio observations. Comparing to the best matched simulation results in Figure 9, and allowing for the slightly ellipsoidal shape of the observed CO clouds, we identify the current positions of the clusters in the CO observations and their recent trajectory and shown this in the right subfigure of Figure 11. The small cluster coincides roughly with the second CO peak (W2 in Figure 6) and the large cluster with the main radio peak. This reflects the cluster densities; the small cluster is denser even before the collision and the discrepancy increases in the interaction. The ionized gas traced by radio and [S IV] emission peaks close to the large cluster and extends into the "bridge" area in the CO clouds (W3-W4 in Figure 6), consistent with greater number of stars and higher ionization rate of the large cluster. The trajectory deduced for the smaller cluster, shown by the blue arrow,

allows us to reconstruct the history of the collision. The smaller cluster grazes the large cluster, this collision lowering the average density of the large cluster and deforming the gas distribution. The smaller cluster, which is more compact and has a higher average density (see Figure 8), also deforms slightly but less than the large cluster. The ionization observed in the "bridge" raises the interesting possibility that a new SSC could form in the filament/band formed by the gas exchange between the clusters. This filament/band is at high pressure and density and as critical line mass depends on the width (Hacar et al. (2022)) it may fragment easily; stars can form in such conditions rapidly, matching the simulation timespan of a few hundred Kyr. In this grazing collision, however, large shear forces are generated that may work against filament collapse and fragmentation.

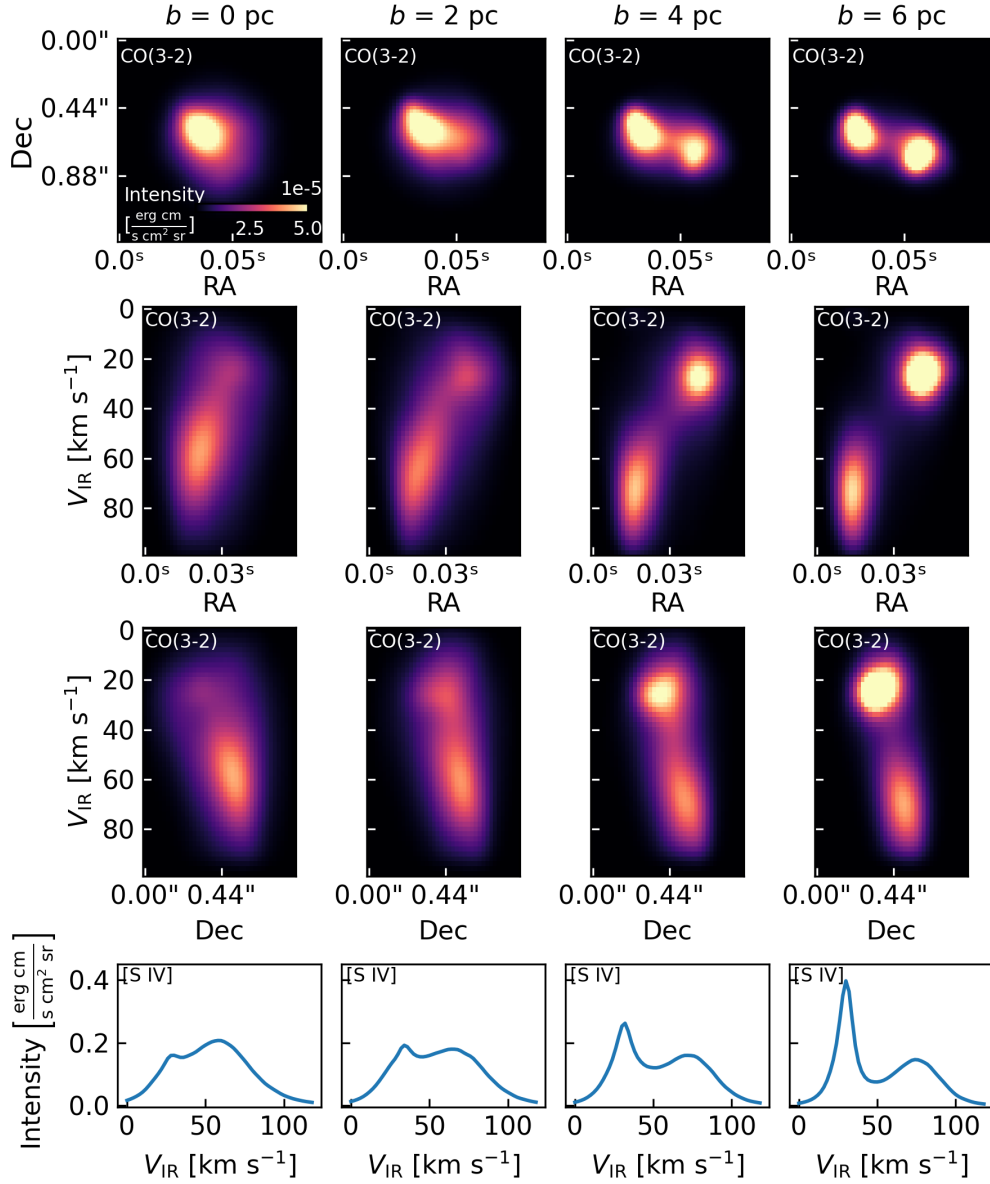


Figure 10. Results of the line profile simulations for the CO(3-2) and [S IV] lines at a fixed observation inclination angle of 45° at $T = 0.5\text{Myr}$, where each column shows the results for a different impact parameter. The CO(3-2) moment map and PVDs were convolved with the beam size of the observations (the intensity scale was $[1,5] \times 10^{-5}$ $\text{erg s}^{-1} \text{cm}^{-2} \text{sr}^{-1} \text{cm}$). Top row shows the 0^{th} moment maps, middle rows show the PVDs along the Dec and RA axes, and the bottom row shows the line profile for [S IV].

The clusters in this collision are not gravitationally bound to each other; if no new SSC forms the bridge area between the clusters (W3) will thin out until the two clusters separate completely.

Finally, we note that based on the [S IV] and CO distribution seen in Figure 11 the small cluster appears to lie on the outer region of the [S IV] distribution, which could indicate that it contains a much smaller amount of stars that were formed prior to collision. We believe that this is due to the small cluster ionizing less of the surrounding gas due to its higher density, combined with the lower resolution of the [S IV] observations compared to the CO, resulting in the [S IV] peak being closer to the large cluster core. Alternatively, this could be due to the small cluster clump containing no stars prior to the collision, so that only the large clump contained already formed stars. In this

scenario, the small clump's collision distorts the large cluster and reduces its density, so that more of the gas near the large cluster becomes ionized. A third option is the formation of a new SSC in the bridge area between the two cluster cores; for this solution to work it would have to be formed relatively closer to the large cluster's core. This discrepancy between the CO and [S IV] distributions could be solved by obtaining higher resolution observations of the ionized gas, as well as running higher resolution simulations that account for fragmentation, accretion and star formation.

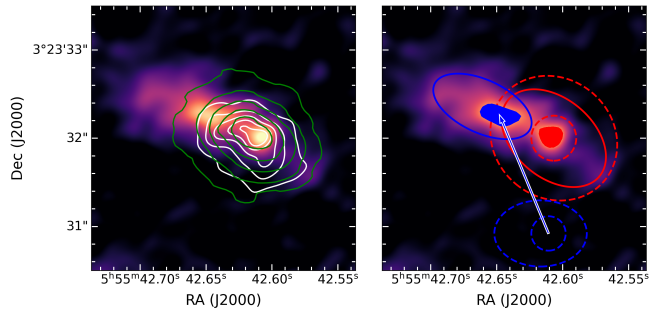


Figure 11. Left: The CO(3-2) MOM0 map overlaid with contours of the naturally weighted 15GHz map in white and the [S IV] MOM0 in green. Right: The CO(3-2) MOM0 map with rough approximations of the sizes and shapes of the small (blue) and large (red) clusters and their cores. They are shown before and after the collision as dotted and solid lines respectively. The blue arrow shows the possible trajectory of the small cluster as it collides with the large cluster.

6.2 Summary and Comments

We have used simulations of colliding star clusters to create a model of the embedded clusters of II Zw 40 that agrees with both the spatial appearance and the kinematics of the ionized gas in the system. The most successful model is summarized in the previous section. We now consider the successes and limitations of the current simulations and the questions that remain unanswered in II Zw 40.

- This project concentrated on the stars and ionized gas associated directly with the clusters. The primary motivation of the models was to understand the unique spectral line profile and structure of the ionized gas on embedded source. The models have been successful at matching the line profiles and position-velocity dependence of the [S IV] data with a simple and physically plausible scenario.

- While the elongated appearance and two-component velocity structure of the molecular gas motivated the models and help establish the velocities of the components, the present simulations do not attempt to model the molecular component nor its interactions with the stars and ionized gas. The kinematic situation of the elongated molecular clouds in II Zw 40 is intriguing. Except directly on the embedded clusters, they appear almost unaffected by the stellar winds and high gas pressures associated with the young stars. The velocity is almost uniform across each and we do not see the shear that would show tidal effects. What will happen as the young star clusters evolve?

- The major unanswered question is whether the star clusters were formed before the collision as we posited here, or are a result of the collision of two clouds. As the upper range of the age of SSC-N is 3Myr [Vanzi et al. \(2008\)](#), both options are at present valid and the simulations cannot at present distinguish. The ratio of molecular gas to stellar mass in this starburst is very low; the $3.5 \times 10^5 M_{\odot}$ of molecular gas [Consiglio et al. \(2017\)](#) find on 'W' and 'C' is less than the stellar mass deduced for the clusters. This argues that star formation has proceeded very rapidly and efficiently to use up most of the available gas; this may have wiped out kinematic signatures that could have been seen in the molecules.

- To simulate the processes of cluster formation will need more models of colliding clumps that include accretion and fragmentation, as well as the interactions of molecular gas with the stellar winds of young stars. Further questions to investigate include the role of the

magnetic field in forming the clumps and controlling the interaction, and the relation of the current starburst to the interaction history of the galaxy.

Theory predicts that collisions and mergers should play a major role in the evolution of star clusters and of the clouds where they form. We have the good fortune to live at exactly the right time to see this short lived interaction stage in II Zw 40, and to have the very high spectral resolution of ALMA and TEXES data to reveal the interaction process. These results show that simulations and models of complex systems will have their greatest power when based on and guided by high resolution data.

7 ACKNOWLEDGEMENTS

- This paper makes use of ALMA data from program 2013.1.00122.S. ALMA is a partnership of ESO (representing its member states), NSF (USA) and NINS (Japan), together with NRC (Canada), NSTC and ASIAA (Taiwan), and KASI (Republic of Korea), in cooperation with the Republic of Chile. The Joint ALMA Observatory is operated by ESO, AUI/NRAO and NAOJ.

- The National Radio Astronomy Observatory is a facility of the National Science Foundation operated under cooperative agreement by Associated Universities, Inc.

- Based on observations obtained in program GN-2017A-Q-57 at the international Gemini Observatory, a program of NSF NOIRLab, which is managed by the Association of Universities for Research in Astronomy (AURA) under a cooperative agreement with the U.S. National Science Foundation on behalf of the Gemini Observatory partnership: the U.S. National Science Foundation (United States), National Research Council (Canada), Agencia Nacional de Investigación y Desarrollo (Chile), Ministerio de Ciencia, Tecnología e Innovación (Argentina), Ministério da Ciência, Tecnologia, Inovações e Comunicações (Brazil), and Korea Astronomy and Space Science Institute (Republic of Korea).

Table 1. Observational Parameters

Date	Telescope	Wavelength	Beam Size	Spectral Channels	noise Jy beam ⁻¹
15/10/16	JVLA	22 GHz	0.12 × 0.07''(briggs wt)	NA	1.6 × 10 ⁻⁵
31/10/16	JVLA	15 GHz	0.2 × 0.1''(briggs wt.)	NA	2 × 10 ⁻⁵
13/08/14	ALMA	345 GHz	0.34 × 0.25''	2 km s ⁻¹	3.5 × 10 ⁻⁵
13/12/14	ALMA	345 GHz	"	"	"
15/03/17	Gemini North	10.5 μm	0.3 × 0.3''	0.95 km s ⁻¹	5 × 10 ⁻³ erg s ⁻¹ cm ⁻² sr ⁻¹ cm

8 DATA AVAILABILITY

The data used in this paper are available to the public at the archives of the observatories where they were obtained: the radio continuum data is on the NRAO archive, the molecular data at the ALMA archive, and the [S IV] data is at Gemini North.

REFERENCES

- Beck S. C., Turner J. L., Langland-Shula L. E., Meier D. S., Crosthwaite L. P., Gorjian V., 2002, *AJ*, **124**, 2516
- Beck S., Turner J., Lacy J., Greathouse T., Lahad O., 2013, *ApJ*, **767**, 53
- Bordalo V., Plana H., Telles E., 2009a, *Astrophys.J.*, 696, 1668
- Bordalo V., Plana H., Telles E., 2009b, *ApJ*, **696**, 1668
- Consiglio S. M., Turner J. L., Beck S., Meier D. S., 2016, *ApJ*, **833**, L6
- Consiglio S. M., Turner J. L., Beck S., Meier D. S., Silich S., Zhao J.-H., 2017, *ApJ*, **850**, 54
- Dolcetta R. C., Sedda M. A., Battisti A. M., Punzo D., Spera M., 2011, ASP Conf. Series, 2012, vol. 453
- Dullemond C. P., Juhasz A., Pohl A., Sereshti F., Shetty R., Peters T., Commercon B., Flock M., 2012, Astrophysics Source Code Library, 1202.015
- Fujii M., Iwasawa M., Funato Y., Makino J., 2007, *PASJ*, **59**, 1095
- Fukui Y., et al., 2016, *ApJ*, **820**, 26
- Habe A., Ohta K., 1992, *PASJ*, **44**, 203
- Hacar A., Clark S., Heitsch F., Kainulainen J., Panopoulou G., Seifried D., Smith R., 2022, Protostars and Planets, VII
- Kepley A. A., Reines A. E., Johnson K. E., Walker L. M., 2014, *AJ*, **147**, 43
- Kepley A. A., Leroy A. K., Johnson K. E., Sandstrom K., Chen C.-H. R., 2016, *ApJ*, **828**, 50
- King I. R., 1966, *Astronomical Journal*, Vol. 71, p. 64 (1966), 71, 64
- Lacy J. H., Richter M. J., Greathouse T. K., Jaffe D. T., Zhu Q., 2002, *PASP*, **114**, 153
- Lada C. J., Lada E. A., 2003, *Annual Review of Astronomy and Astrophysics*, **41**, 57
- Leitherer C., Byler N., Lee J. C., Levesque E. M., 2018, *ApJ*, **865**, 55
- Mould J. R., et al., 2000, *ApJ*, **529**, 786
- Pelupessy F., Portegies Zwart S., 2012, *Monthly Notices of the Royal Astronomical Society*, **420**, 1503
- Plummer H. C., 1911, *Monthly Notices of the Royal Astronomical Society*, Vol. 71, p. 460-470, 71, 460
- Portegies Zwart S., McMillan S., 2018, *IOP*, pp 3–1 to 3–37
- Sage L. J., Salzer J. J., Loose H. H., Henkel C., 1992, *A&A*, **265**, 19
- Salpeter E. E., 1955, *Astrophysical Journal*, vol. 121, p. 161, 121, 161
- Sargent W. L. W., Searle L., 1970, *ApJ*, **162**, L155
- Searle L., Sargent W. L. W., 1972, *ApJ*, **173**, 25
- Spitzer L., 1987, *Dynamical evolution of globular clusters*, Princeton, NJ, Princeton Univ
- Springel V., 2005, *Mon.Not.Roy.Astron.Soc.*, **364**, 1105
- Springob C. M., Haynes M. P., Giovanelli R., Kent B. R., 2005, *ApJS*, **160**, 149
- Takahira K., Shima K., Habe A., Tasker E. J., 2018, *PASJ*, **70**, S58
- Torii K., et al., 2017, *ApJ*, **835**
- Vanzi L., Cresci G., Telles E., Melnick J., 2008, *A&A*, **486**, 393
- Wu Y., Charmandaris V., Hao L., Brandl B. R., Bernard-Salas J., Spoon H. W. W., Houck J. R., 2006, *ApJ*, **639**, 157
- Wunsch R., Silich S., Palous J., Tenorio-Tagle G., Munoz-Tunon C., 2011, *ApJ*, **740**, 75
- van Zee L., Haynes M. P., Giovanelli R., 1995, *AJ*, **109**, 990
- van der Helm E., Saladino M. I., Zwart S. P., Pols O., 2019, *A&A*, **625**, A85

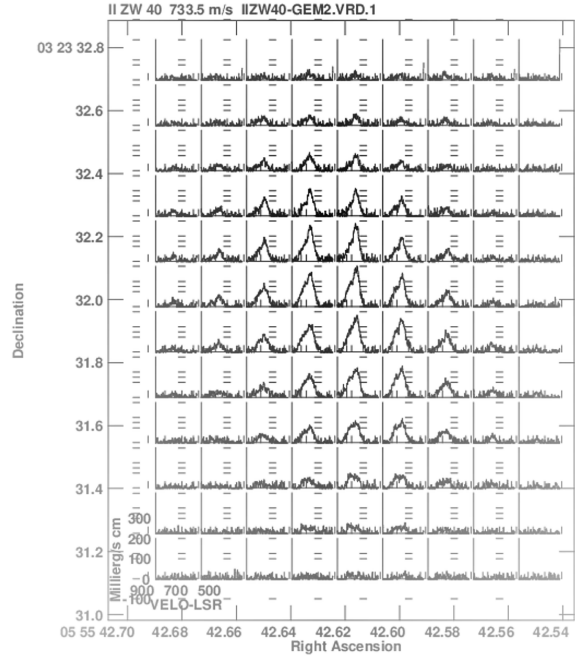


Figure 12. The [S IV] spectrum, Hanning smoothed, in every spatial pixel in the II Zw 40 emission region. Velocity is in km s^{-1} .

9 APPENDIX

9.1 [S IV] Spectral Line Profiles

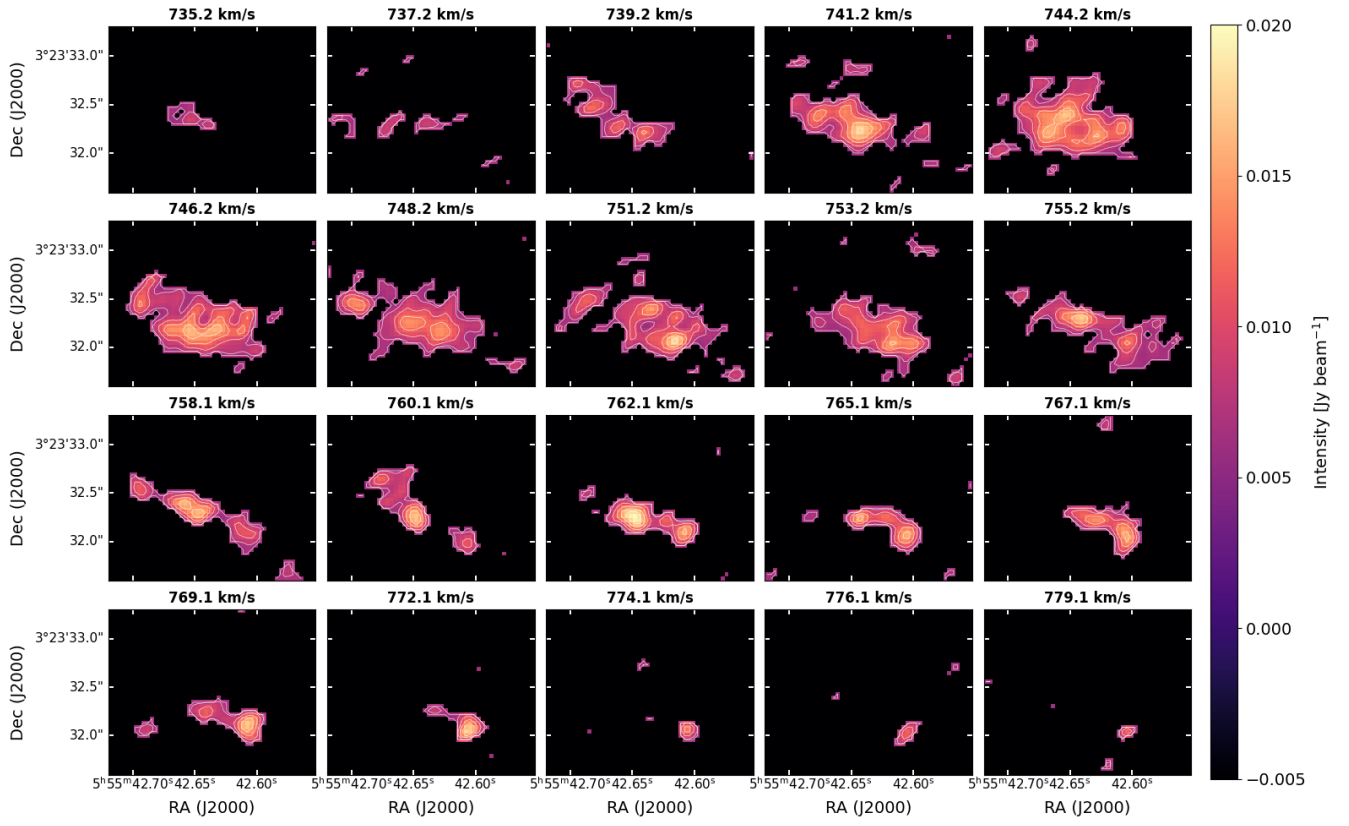


Figure 13. Channel maps of the CO(3-2) observations. The contours are at [0.005, 0.0075, 0.01, 0.0125, 0.015, 0.0175, 0.02] Jy beam⁻¹.

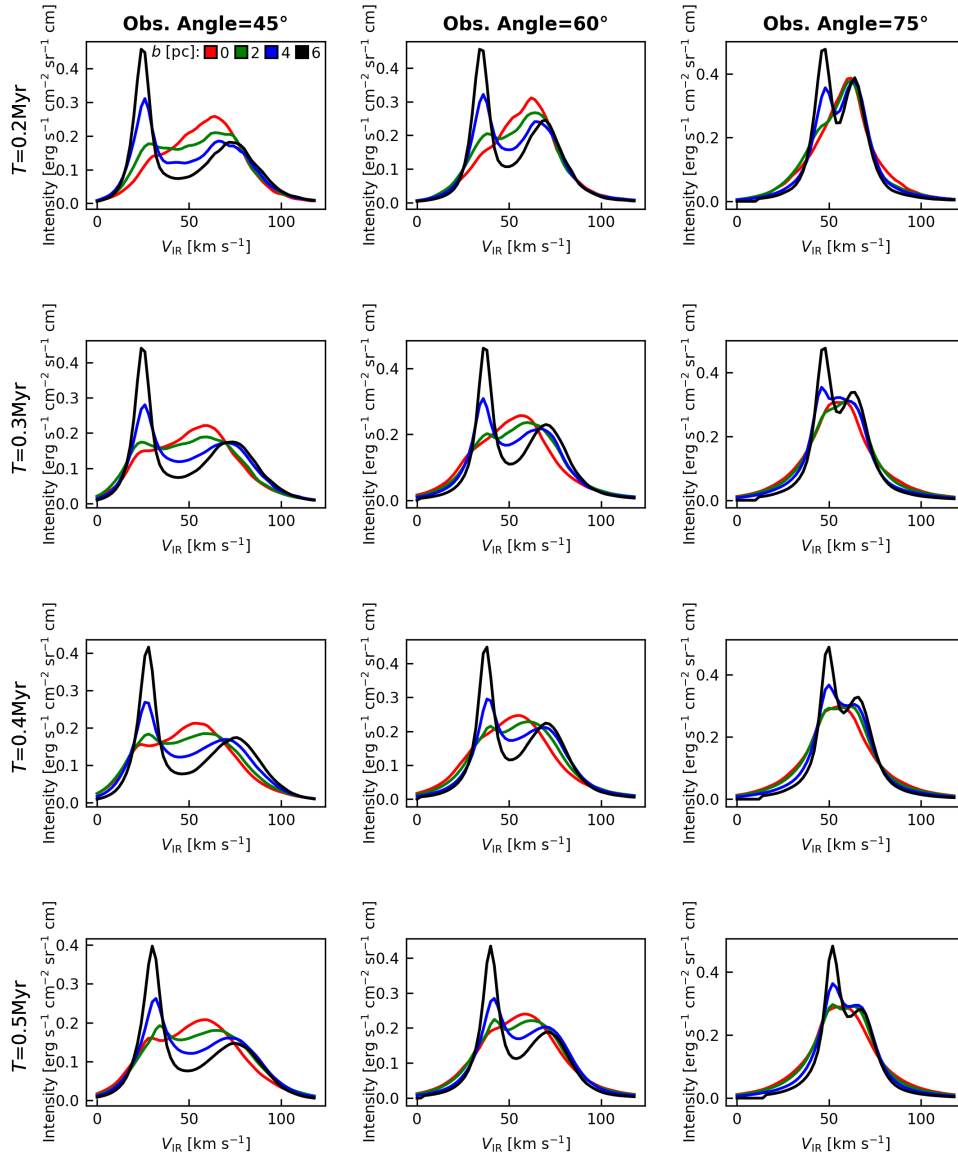


Figure 14. [S IV] line profile simulation results for multiple impact parameters, where each row corresponds to a different timestep and each column corresponds to a different observation inclination angle.